



Article

Compositional Effects on Mechanical Performance of Zirconia–Magnesia–Alumina Ceramics

Rafael Shakirzyanov ^{1,2} , Sofiya Maznykh ^{1,2}, Yuriy Garanin ^{1,2} and Malik Kaliyekperov ^{1,2,*} 

¹ Engineering Profile Laboratory, L.N. Gumilyov Eurasian National University, Satpayev St., Astana 010008, Kazakhstan; shakirzyanov_ri@enu.kz (R.S.); sofiyamaznykh@gmail.com (S.M.); garanin_yua_1@enu.kz (Y.G.)

² Laboratory of Solid State Physics, The Institute of Nuclear Physics, Almaty 050032, Kazakhstan

* Correspondence: kaliyekperov_mye_2@enu.kz; Tel.: +7-708-626-48-93

Abstract

The study of the relationship between the composition and mechanical properties of structural ceramics based on zirconium, magnesium and aluminum oxides is an important scientific and technological task. In this study, ceramics of the composition $x\text{-ZrO}_2\text{-(90-x)-MgO-10-Al}_2\text{O}_3$ ($x = 10\text{--}80$ wt.%) were obtained using standard ceramic technology. XRD, SEM, Vickers hardness and biaxial flexural strength measurements were performed to determine the effect of concentration x on the phase composition, microstructure and mechanical characteristics of the sintered samples. The results show that with an increase in the starting concentration x in experimental samples, the fraction of the stabilized ZrO_2 phase grows, and the grain size decreases. These two factors determine the values of microhardness and biaxial bending strength. Experimental investigation on the ternary oxide ceramics shows that for ceramics sintered at 1500°C , the microhardness values varied within the range of 815–1300 HV1 and the biaxial bending strength of 110–250 MPa.

Keywords: alumina; zirconia; composite ceramics; microhardness; flexural strength



Academic Editor: Malika Saadaoui

Received: 21 August 2025

Revised: 12 September 2025

Accepted: 15 September 2025

Published: 17 September 2025

Citation: Shakirzyanov, R.; Maznykh, S.; Garanin, Y.; Kaliyekperov, M. Compositional Effects on Mechanical Performance of Zirconia–Magnesia–Alumina Ceramics. *Ceramics* **2025**, *8*, 114. <https://doi.org/10.3390/ceramics8030114>

Copyright: © 2025 by the authors. Licensee MDPI, Basel, Switzerland. This article is an open access article distributed under the terms and conditions of the Creative Commons Attribution (CC BY) license (<https://creativecommons.org/licenses/by/4.0/>).

1. Introduction

In modern industry, technology, and medicine, engineering structural ceramics occupy an important place, and their advantages are their high thermal resistance, mechanical strength, and chemical inertness [1–3]. Among others, ceramics based on Al_2O_3 , ZrO_2 , and their composites stand out [4,5]. Due to their unique mechanical, thermal, optical and electrical properties, these types of ceramics are used as refractory materials [6], structural materials for work in aggressive environments [7], and have uses in the energy sector and as biomedical materials [8].

Alumina-based ceramics have been among the most readily available and widely used ceramic materials for many years due to their high hardness, high modulus of elasticity, chemical resistance and abrasion resistance [9]. The weak points of Al_2O_3 ceramics include low bending strength and resistance to cracking, which limits their use under conditions of higher mechanical loads [10,11]. Zirconium ceramics, in turn, are known for their unique mechanical properties, such as high hardness, heat resistance, and resistance to cracking due to the mechanism of transformation hardening caused by the phase transition from the tetragonal to the monoclinic phase ($t \rightarrow m$ transition) [12–14]. However, pure ZrO_2 is subject to phase transformations with volumetric change, which can cause microcracks and destruction of the material upon cooling [15].

To stabilize high-temperature phases at room temperature, additives of Y_2O_3 [16], CaO [17], and MgO [18] oxides and rare earth elements [19,20] are used. Yttrium-stabilized zirconium (YSZ), the most studied material of this class, has high mechanical strength, but its application is limited by its high cost [21]. Magnesium oxide stands out as an economical and technologically convenient option, providing an extension of the stability range of t-ZrO_2 and a reduction in the effects of hydrothermal aging characteristic of Y-TZP [22].

Composites based on the $\text{ZrO}_2\text{-MgO-Al}_2\text{O}_3$ system are of wide interest due to the fact that the magnesium oxide in it simultaneously promotes the stabilization of t-ZrO_2 at room temperature and improves the sinterability of Al_2O_3 , and also reacts with Al_2O_3 to form a MgAl_2O_4 spinel, which ensures the formation of a microstructure with a controlled grain size, which further improves crack resistance [23,24]. It is noted that magnesium oxide can stabilize t-ZrO_2 not only directly through the introduction of Mg^{2+} ions into the crystal lattice, but also due to the formation of an amorphous $\text{MgO-Al}_2\text{O}_3$ matrix, which limits the growth of ZrO_2 grains and ensures stability up to 1200°C [25].

An additional factor that has a significant impact on the properties of ceramics is the particle size of the magnesium oxide used as a dopant [26]. In [27], it was shown that the use of MgO nanoparticles (about 80 nm in size) promotes the accelerated sintering of ceramics and the formation of a denser and more uniform microstructure, which has a positive effect on the maximum microhardness of the samples. At the same time, excessive particle size reduction is accompanied by a decrease in crack resistance associated with the agglomeration of nanoparticles and their uneven distribution in the volume of the material. It is noted that the optimal particle size of the MgO dopant is critical to achieve balanced mechanical properties of the composite.

Despite significant progress in the study of $\text{ZrO}_2\text{-MgO-Al}_2\text{O}_3$ ceramics, some aspects remain insufficiently studied. In particular, optimization of the component ratio and temperature treatment conditions are important to achieve a balance between the mechanical characteristics of the obtained composite ceramics. For example, researchers K.L. Meena et al. [28] note that sintering temperatures above 1300°C can lead to a decrease in the strength of $\text{ZrO}_2\text{-MgO-Al}_2\text{O}_3$ ceramics as a result of overheating and grain growth, which also emphasizes the importance of temperature control during annealing. In addition, the study of possible phase transformations, spinel formation and degradation of t-ZrO_2 at high temperatures is a promising direction for further research to develop a material with improved characteristics [29].

This work is devoted to the synthesis of composite ceramics $x\cdot\text{ZrO}_2\text{-(90-x)}\cdot\text{MgO-10}\cdot\text{Al}_2\text{O}_3$ in order to study their microstructure, phase composition and mechanical properties. Despite the wide application of $\text{ZrO}_2\text{-MgO-Al}_2\text{O}_3$ ternary oxide ceramics, there is a lack of comprehensive property–composition–structure studies in the scientific literature for this system. It is known that the ternary system $\text{ZrO}_2\text{-MgO-Al}_2\text{O}_3$ has metastable phases that can significantly change properties such as hardness and strength. As mentioned above, the formation of the MgAl_2O_4 spinel can positively influence the formation of the microstructure of ZrO_2 ceramics. By introducing a fixed concentration of Al_2O_3 , this work investigates the effect of corundum additive on the known binary system $\text{ZrO}_2\text{-MgO}$. The main focus of the research is on the study of the formation of metastable phases, such as c-ZrO_2 and t-ZrO_2 , and their influence on the mechanical characteristics of $x\cdot\text{ZrO}_2\text{-(90-x)}\cdot\text{MgO-10}\cdot\text{Al}_2\text{O}_3$ ceramics. Also, zirconium oxide and magnesium oxide are more refractory materials than corundum. For this reason, the work examines the variation in concentrations between ZrO_2 and MgO with a low content of aluminum oxide. The results of this study are extremely important for the creation of new types of refractories with variable thermodynamic and mechanical characteristics.

2. Materials and Methods

For the synthesis of ceramics from a mixture of oxides $x \cdot \text{ZrO}_2 - (90 - x) \cdot \text{MgO} - 10 \cdot \text{Al}_2\text{O}_3$, where $x = 10, 20, 30, 40, 50, 60, 70, 80\%$ (mass concentration of initial component ZrO_2), a standard ceramic technology was chosen. ZrO_2 , MgO , and Al_2O_3 (Sigma Aldrich, 99.99% purity) were mixed in a Pulverisette 6 planetary mill (Fritsch, Idar-Oberstein, Germany) with tungsten carbide (WC) grinding sets for 30 min at a speed of 250 rpm. To obtain homogeneous compositions, ethanol was added to the mass of dry powders before milling. After mixing, the mixture was dried in a drying cabinet at a temperature of 45 °C for several hours to remove all ethyl alcohol from the composition after milling. To initiate the formation of new phases, the resulting dried powders were pre-annealed at a temperature of 1300 °C for 5 h in a Nabertherm LHT 08/18 muffle furnace (Nabertherm, Lilienthal, Germany) in an air atmosphere in corundum crucibles (“Alita” LLP, Ust-Kamenogorsk, Kazakhstan). After the first annealing, powder X-ray diffractometry (XRD) was performed on a Rigaku SmartLab diffractometer (Rigaku, Tokyo, Japan) to determine the phase compositions using the PDF-2 2024 database. The sintered powders were ground in an ethyl alcohol medium in a Pulverisette 7 premium line planetary micromill (Fritsch, Idar-Oberstein, Germany) at 400 rpm for 30 min using a tungsten carbide grinding jar and grinding balls (Fritsch, Idar-Oberstein, Germany) (grinding ball diameter Ø 1.6 mm). At the outlet, the obtained suspension was analyzed for particle size distribution using a laser particle meter Analysette 22 MicroTec (Fritsch, Idar-Oberstein, Germany) plus with a liquid dispersion unit. Polyvinyl alcohol (PVA) (Sigma Aldrich, 95%, Darmstadt, Germany) was chosen as a plasticizer for the production of green powders. The powders were poured into a hot aqueous solution of PVA at ~90 °C and stirred using a magnetic anchor IKA C-MAG HS7 (IKA-Werke GmbH & Co. KG, Staufen, Germany). Then the pre-dried pressed powders were ground in an agate mortar until a homogeneous powder without obvious large agglomerates was obtained. The collected green powders were completely dried in a drying cabinet at a temperature of 90 °C for 10 h. The concentration of PVA in the finished green powder was 2% of the mass of the synthesized powders. To obtain experimental green tablets, the required amount of powder was poured into a hardened stainless steel mold, previously lubricated with oil. The mold for pressing was placed in an automatic hydraulic press (Paratus, Yekaterinburg, Russia) and a pressure of 5 tons was applied from above to the punch for 5 s, and the same time for 10 tons. Tablets with a diameter of Ø 20 mm and a thickness of 1.5 mm were obtained after pressing. The geometrical parameters of disks after sintering are listed in Supplementary Table S1. Geometrical density was calculated by using measured geometrical parameters of disks and measured mass of the ceramic disks. Archimedes density was calculated after crushing a ceramic disk into pieces with a length of 2–3 mm by using a picnometer and deionized water.

The PVA binder was removed from the ceramic composition by preliminary annealing in a muffle furnace with heating at a rate of 1.6 °C/min and holding at 500 °C for 2 h. The final annealing of the tablets was performed in a Nabertherm LHT 08/18 resistance furnace (Nabertherm, Lilienthal, Germany) in an air atmosphere in corundum crucibles at a temperature of 1500 °C for 5 h. A repeated X-ray phase analysis of the samples after sintering was carried out on the sintered final tablets, which was necessary to determine the formed phases. The microstructure of the sample surface and the elemental composition were studied using a Thermo Fisher Phenom X electron microscope (Thermo Fisher Scientific, Eindhoven, The Netherlands) by acquiring backscattered electron images (accelerating voltage 10 and 15 kV, working distance 8.720 mm). The Vickers method was used to determine the microhardness using a Dupoline-M1 microhardness tester (Duroline-M METKON instruments, Bursa, Turkey) with a load of 1000 gf and dwell time of 10 s in 5 random areas. During the measurements, it was observed that the diamond pyramidal

indenter created indentations covering different grains, so the values of microhardness can be considered as effective values of the composite (see illustrations in Supplementary Figure S19). Prior to microhardness tests, the surfaces of the samples underwent a grinding process on a Tegramin (Struers, Ballerup, Denmark) unit with diamond disks of different roughness and diamond paste. The mechanical strength of the tablets was determined by calculating the biaxial flexural strength [30] (ISO 6872, piston-on-three-ball), which was determined by the formula

$$\sigma_{flex} = \frac{3(1+\nu)P}{4\pi t^2} \left[1 + 2\ln \frac{a}{b} + \frac{(1-\nu)}{(2+\nu)} \left(1 - \frac{b^2}{2a^2} \right) \frac{a^2}{R^2} \right] \quad (1)$$

where σ_{flex} is the biaxial bending strength,

P—the load in N;

ν —Poisson's ratio (0.305);

t—the tablet thickness;

a—the radius of the circle on which the spherical supports are located;

b—the radius of the pin pressing on the tablet;

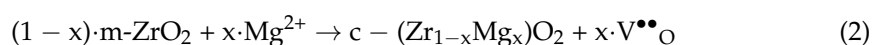
R—the radius of the ceramic tablet.

The test fixture for flexural strength used in the study had the following values of geometrical parameters: $a = 6.5$ mm, $b = 1.13$ mm. The disk compression tests were carried out on a universal electromechanical single-column WalterBai LFM-L 10 kN machine (WalterBai, Lohningen, Switzerland) with a crosshead speed of 0.05 mm/s by compression of 3 disks of the same composition. The sample was mounted on spherical supports, and a movable metal pin was moved from above until the tablet was destroyed.

3. Results and Discussion

Figure 1a shows the particle size distributions after pre-annealing and milling. The distribution histograms are asymmetrical, and the particle sizes range from 0.1 to 5 μm . The wider distribution for samples with a concentration of $x = 10, 20$ wt.% is explained by the large size of agglomerates for the MgO particles, which were used as the starting material (Figures S1c,d and S2b). This may also be due to the solid state reaction occurring with particle coarsening. In addition, at low zirconium oxide concentrations, there is good contact between MgO particles, which apparently leads to better sinterability. With an increase in the ZrO_2 concentration, the sinterability of MgO and Al_2O_3 particles deteriorates, since neither MgO nor Al_2O_3 form new compounds with ZrO_2 under pre-annealing conditions [31]. Also, the size of the initial ZrO_2 powder was less than 1 μm , which determined the small size and narrow distribution of the pre-annealed particles. The dependence of the average particle size on the starting concentration x is shown in Figure 1b. The increase in the average particle size at the last concentration $x = 80$ wt.% can also be associated with better sinterability of the zirconium dioxide particles, which constitute the basis of the mixture.

Figure 2 reveals the XRD patterns for all pre-annealed powders. The main phases on the figure are depicted by special symbols, and dotted drop lines were added to indicate the peaks of each phase. The XRD patterns show the presence of peaks of four main phases: monoclinic zirconia m- ZrO_2 , periclase (magnesium oxide), spinel MgAl_2O_4 and stabilized cubic zirconia c- $(\text{Zr}_{1-x}\text{Mg}_x)\text{O}_2$. It can be stated that during pre-annealing in the $x\cdot\text{ZrO}_2$ -(90- x)-MgO-10 $\cdot\text{Al}_2\text{O}_3$ mixture, the following solid-state chemical reactions occur [32]:



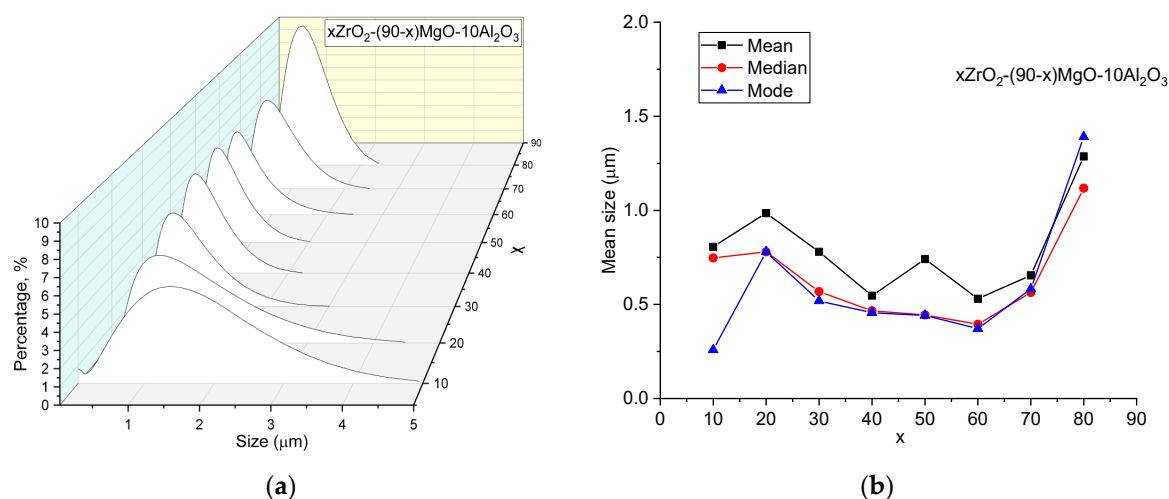


Figure 1. Size distribution of milled powders after pre-annealing at 1300 °C (a) and the dependence of mean and median sizes and modes of distributions from starting concentration x (b).

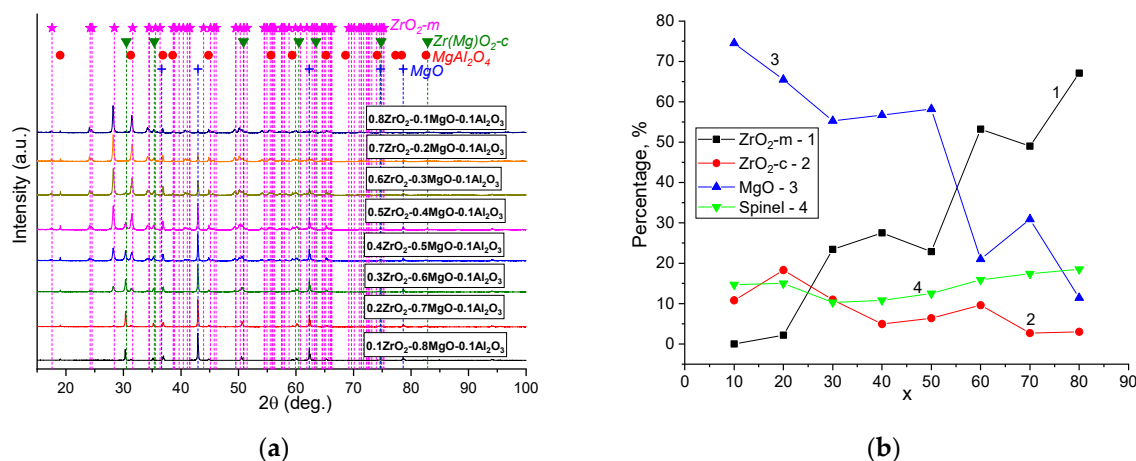


Figure 2. XRD patterns (a) and phase composition of powders after preliminary annealing (b).

A full-profile analysis was performed on the experimental diffraction patterns using the Rietveld method [33]. Statistical parameters of fitting, such as R_{wp} and R_p , were in the range of 6.88–8.61 and 5.19–6.71, respectively. The results of the analysis are presented as dependences of the concentration of each of the above-mentioned phases on the concentration x (Figure 2b). Some discrepancies in the phase composition according to the diffraction pattern analysis from the nominal composition of the batch are explained by the high adsorption coefficient of X-rays of magnesium oxide. From the obtained dependencies it is important to highlight that the proportion of stabilized zirconium dioxide is within 5–18 wt.%. This indicates an insufficient temperature for the formation of substituted stabilized zirconium dioxide.

The density and volume shrinkage of the tablets sintered at 1500 °C were estimated by measuring the thickness, diameter, and weight before and after sintering. The results of the density and shrinkage calculations are shown in Figure 3a,b. As is evident from Figure 3a, the density of the sintered ceramic tablets increases as the concentration x grows according to a linear relationship. This tendency of the curve can be explained by the fact that the composition of the ceramics changes in such a way that the component with a lower physical density (periclase, MgO) is substituted by a component with a high density (ZrO_2). Volume shrinkage, on the other hand, decreases with increasing concentration x, and on the curve one can distinguish two slopes, which can correspond to different sintering mechanisms. Explanations for this will be given below.

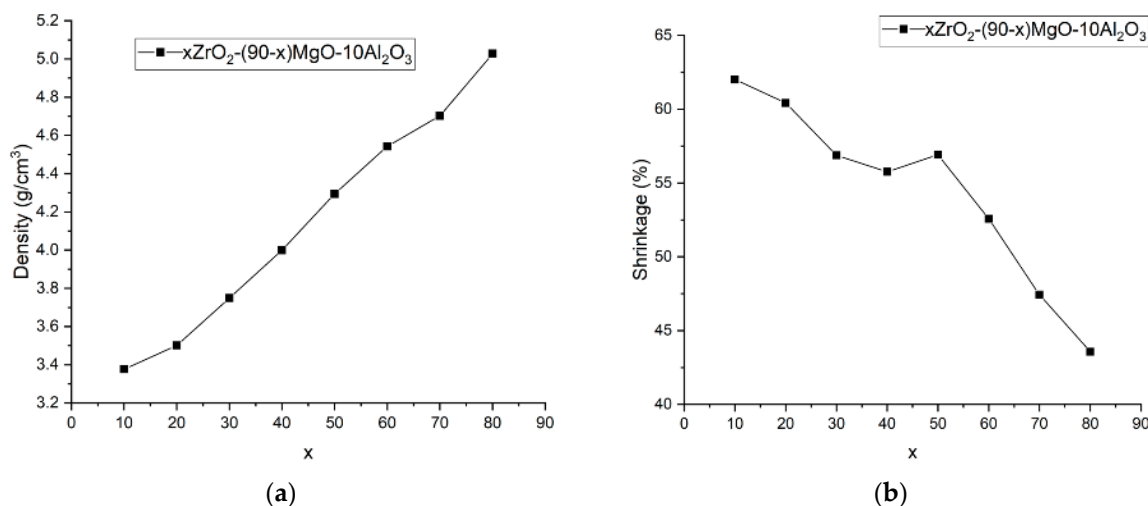


Figure 3. Dependence of apparent density (a) and volume shrinkage (b) on x.

The XRD patterns in the $2\theta = 15\text{--}100^\circ$ range of the sintered tablets are shown in Figure 4a. To clarify the main features, XRD patterns were also plotted in the $2\theta = 20\text{--}50^\circ$ range in Figure 4b and separately in the Supplementary Files (Figures S3–S10). As can be seen from Figure 4a,b, the XRD patterns show reflections from the periclase phases, magnesium–aluminum spinel, and monoclinic zirconium, as well as cubic and tetragonal zirconium dioxide. Small peaks of the secondary phases of silica, CaWO_4 and Mg_2SiO_4 also are presented in the XRD pattern due to possible contamination from the corundum crucible or muffle lining. The intensities of the reflections corresponding to the c- ZrO_2 phases are significantly higher compared to the diffraction patterns recorded on pre-annealed powders, indicating an intense reaction (2) at 1500°C . An unexpected result is that for the sample with a concentration of $x = 60$ wt.%, a significant increase in the intensities of the reflections of the monoclinic phase of ZrO_2 is observed. Some XRD patterns show the presence of a CaWO_4 phase, which occurred after the decomposition of tungsten carbide. The tungsten carbide particles contaminated pre-annealed powders during grinding and oxidized with the formation of CaWO_4 .

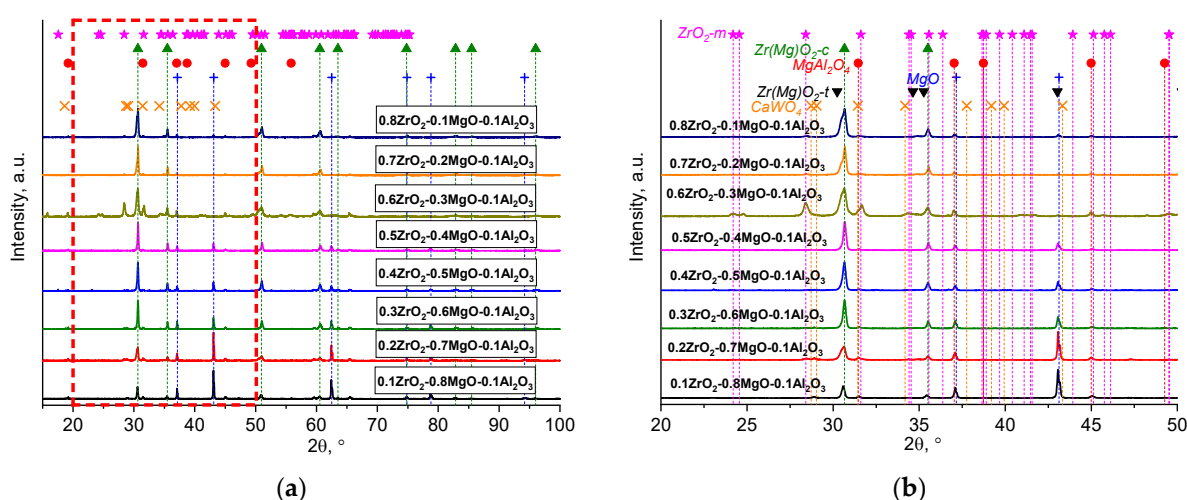


Figure 4. XRD patterns of tablets sintered at 1500°C in the range of angles $15\text{--}100^\circ$ (a) and $20\text{--}50^\circ$ (b).

The microstructure of the sintered tablet's unpolished surface is shown in the SEM images in Figure 5. As can be seen from the images, two contrasting areas can be distinguished—light grains and dark grains. The dark areas correspond to MgO and

Mg-Al spinel grains, while the light ones correspond to the c-ZrO₂ phase. For better illustration, EDX elemental maps are also shown in Supplementary Figures S11–S18. MgO grains are rounded and larger in size, reaching 10 µm at low concentrations, while spinel grains are polygonal. Some micrographs show grains of tungsten oxide or wolframite. The surface of the zirconium dioxide grains, starting with a concentration of $x = 20$ wt.%, has a developed morphology with extended pores, grooves and convolutions. Based on the results of ZrO₂-MgO ceramics, where high-resolution electron microscopy images are available, this type of zirconium dioxide grain is acquired due to the eutectoid decomposition $c\text{-(Zr}_{1-x}\text{Mg}_x)\text{O}_2 \rightarrow m\text{-(1-x)ZrO}_2 + x\text{MgO}$ [34,35]. In addition, high-temperature annealing can cause the volatilization of Mg atoms from the ceramic surface [36]. During the volatilization process, defective regions with a high concentration of vacancies are created, which migrate along the grain surface and form extended voids.

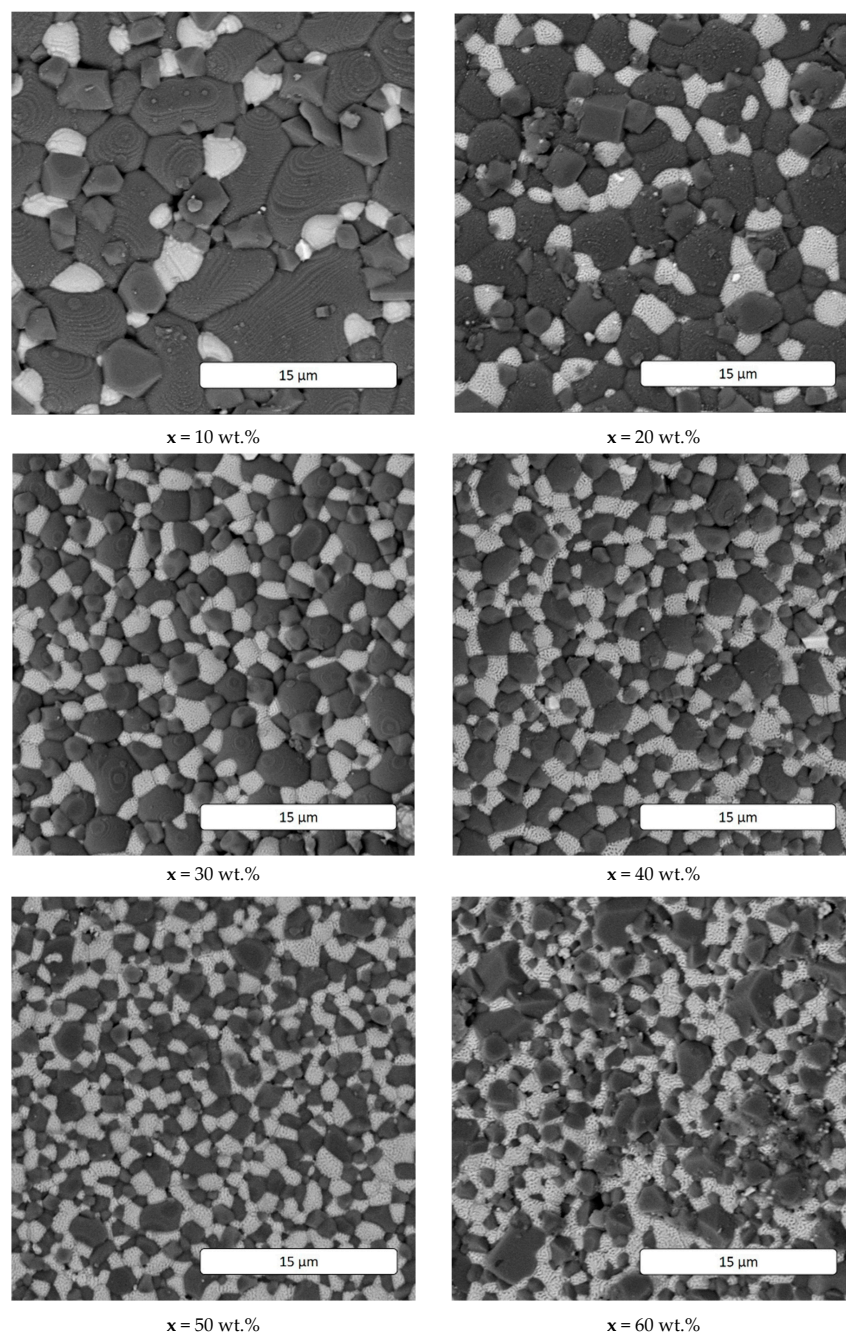


Figure 5. *Cont.*

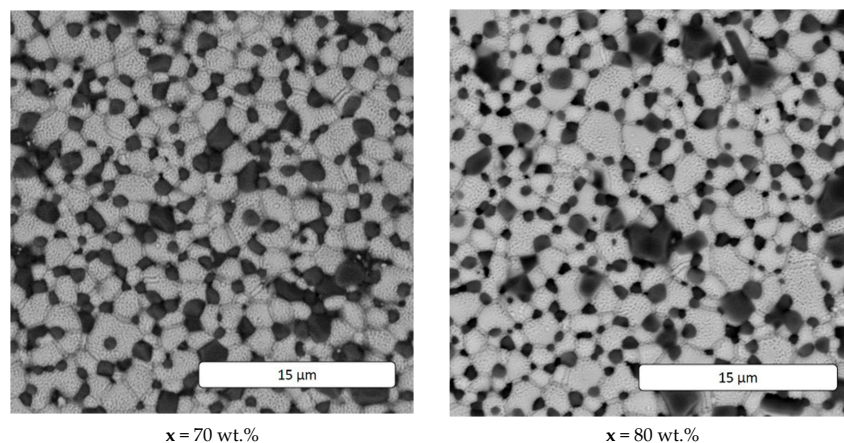


Figure 5. SEM images of the surface of sintered tablets.

As the concentration x increases, the grain size of the zirconia (inclusion phase) grows and the matrix phase $\text{MgO}/\text{MgAl}_2\text{O}_4$ changes places with ZrO_2 and becomes the inclusion phase. The change in grain size distribution with elevation of concentration x can also be traced in the grain size distribution histograms in Figure 6. Samples with a large amount of periclase have wide distributions and high shrinkage values (Figure 3b). As concentration x increases, MgO particles present in the powders can act as inhibitors of zirconium dioxide grain growth [25]. In this case, the shrinkage of the samples will decrease, and the grain size will be smaller than in ceramics with excess MgO .

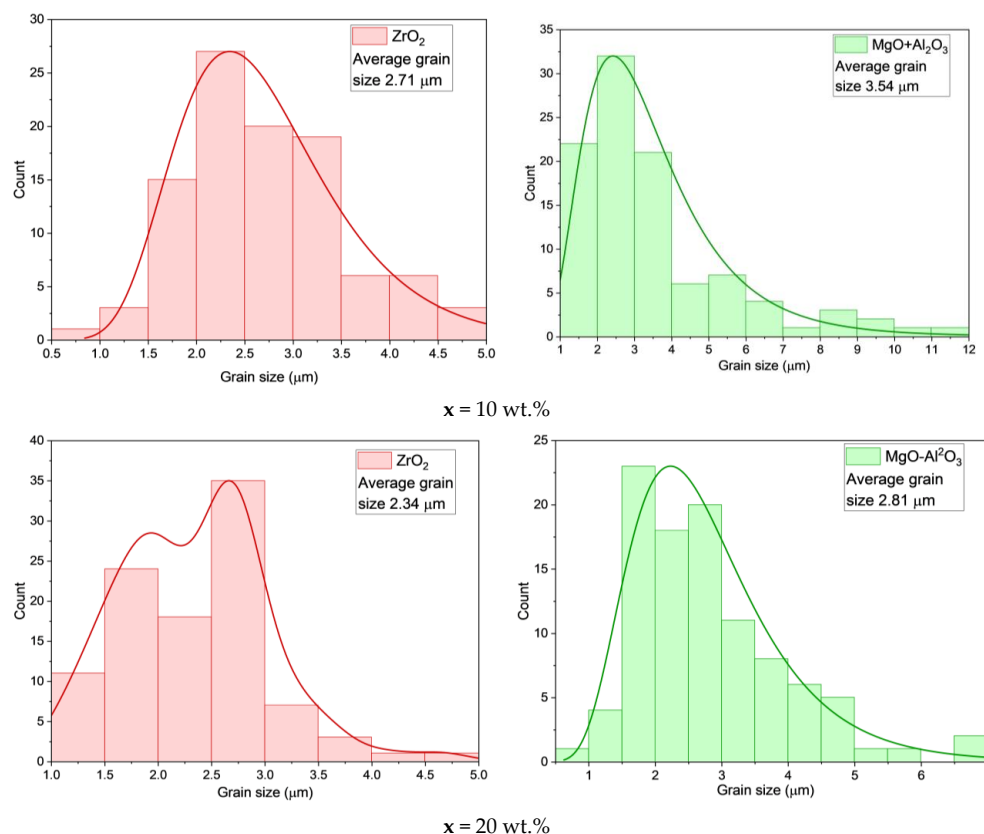


Figure 6. Cont.

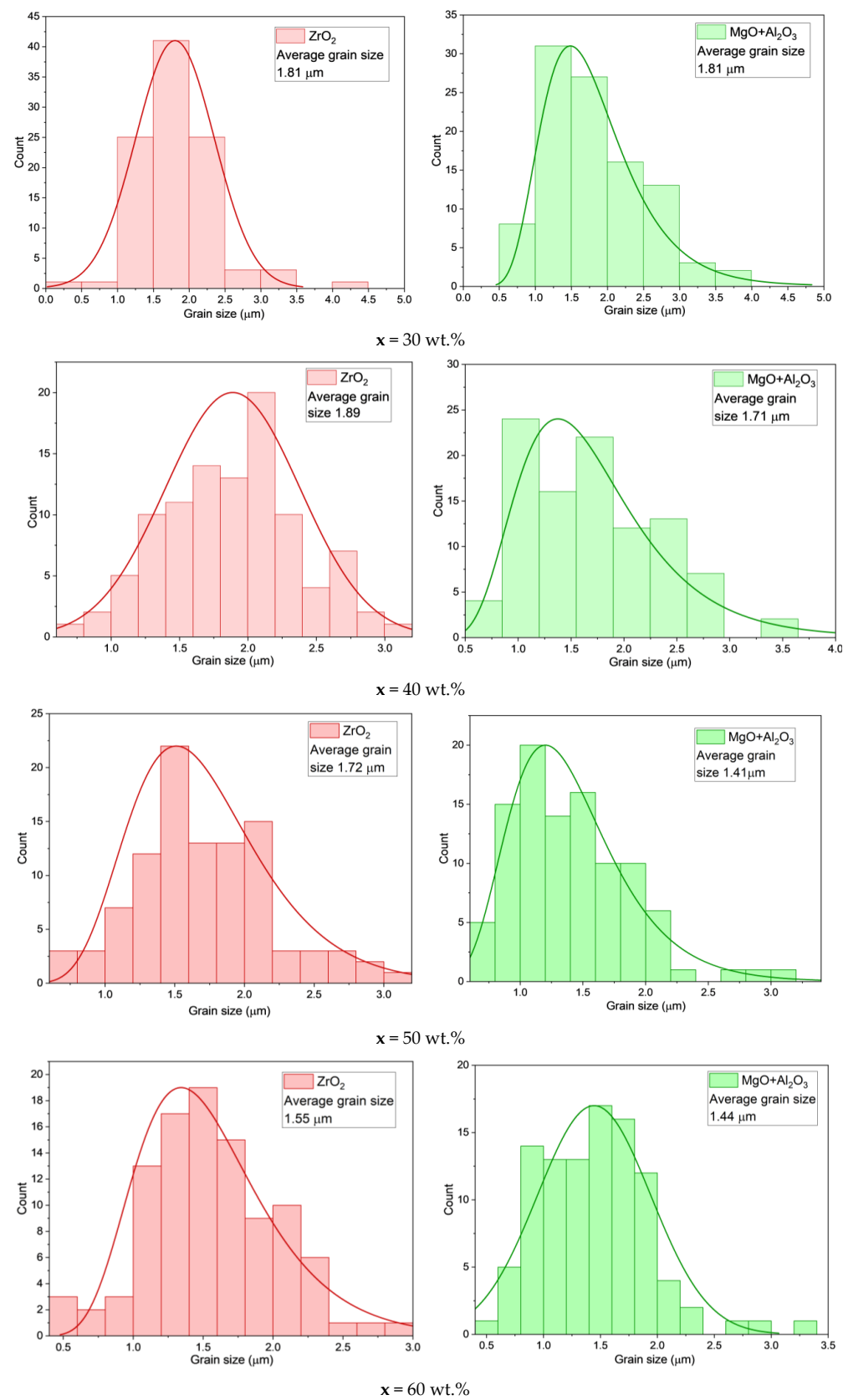


Figure 6. Cont.

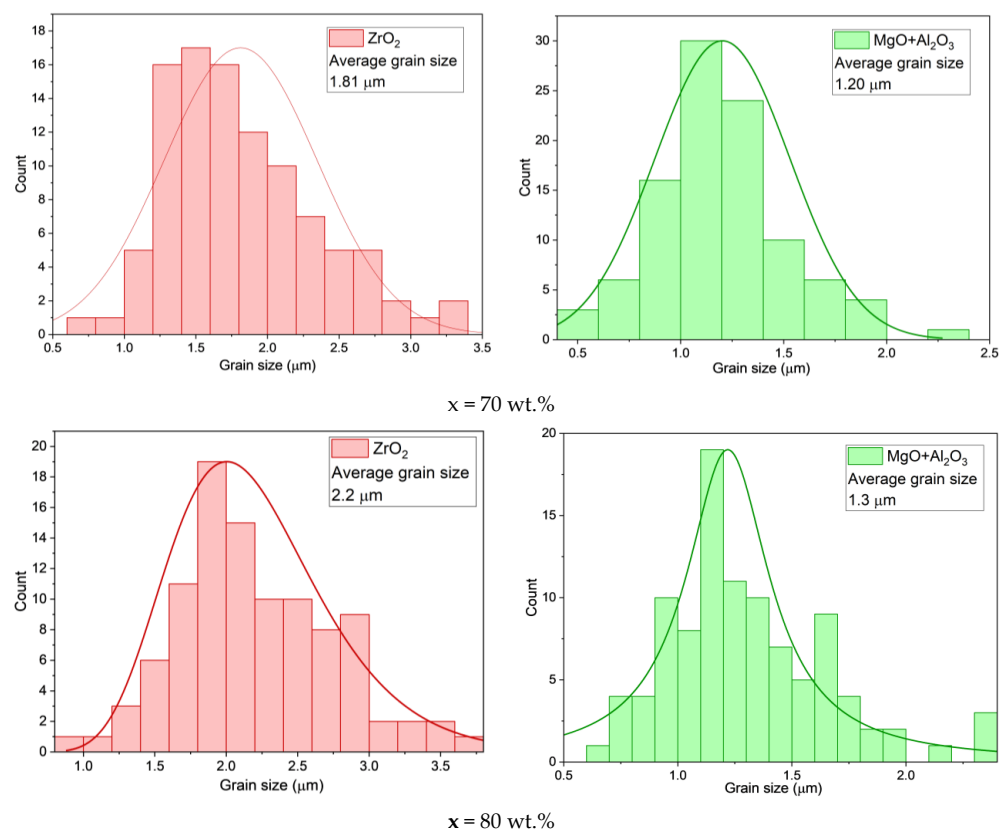


Figure 6. Distribution of grain sizes of zirconium dioxide and MgO, Al₂O₃.

The mechanical characteristics of the sintered ceramics were assessed by measurement of the Vickers microhardness and the biaxial flexural strength. Table 1 illustrates the obtained values of the above characteristics for all concentrations of x . A comparison of these dependences shows that the changes in HV and σ_{flex} have sections with the same characteristic bends. At initial concentrations ($x = 10$ wt.%), a slight increase with a plateau was observed for the HV dependence. For $\sigma_{flex}(x)$, a continuous growth up to the point $x = 50$ wt.% was observed. Such behavior is associated with a change in the phase composition and microstructure.

Table 1. The comparison of phase composition, phase content, statistical parameters of Rietveld refinement, HV microhardness, and σ_{flex} among obtained ceramics.

x , wt. %	Phase Name	Phase Content, %	Statistical Parameters				ρ_{exp} , g/cm ³	Open Porosity, %	HV1	σ_{flex} , MPa
			R_{wp} , %	R_p , %	R_e , %	χ^2				
10	c-ZrMgO ₂	11.53 ± 0.09	8.04	6.02	7.3	1.2106	3.3368	6.86	830 ± 38	122 ± 4.76
	MgO	74.05 ± 0.02								
	MgAl ₂ O ₄	13.09 ± 0.17								
	CaWO ₄	1.33 ± 0.09								
20	c-ZrMgO ₂	12.2 ± 0.03	8.05	6.03	7.3	1.2123	3.5012	5.59	832 ± 51	146 ± 11.41
	MgO	56.7 ± 0.05								
	MgAl ₂ O ₄	18.5 ± 0.02								
	m-ZrO ₂	5.2 ± 0.02								
	t-ZrO ₂	6.21 ± 0.03								
30	CaWO ₄	1.19 ± 0.07	10.49	7.54	6.82	2.3663	3.7488	5.39	898 ± 70	150 ± 6.57
	c-ZrMgO ₂	40.1 ± 0.03								
	MgO	32.2 ± 0.03								
	MgAl ₂ O ₄	26.4 ± 0.04								
	m-ZrO ₂	0.0								
	CaWO ₄	1.30 ± 0.16								

Table 1. Cont.

x, wt. %	Phase Name	Phase Content, %	R_{wp} , %	Statistical Parameters			ρ_{exp} , g/cm ³	Open Porosity, %	HV1	σ_{flex} , MPa
			R_p , %	R_e , %	χ^2					
40	c-ZrMgO ₂	46.3 ± (5)	11.15	7.68	6.69	2.7734	3.9999	5.91	1037 ± 12	208 ± 11.07
	MgO	28.2 ± (4)								
	MgAl ₂ O ₄	13.2 ± (3)								
	CaWO ₄	7.2 ± (6)								
	Mg ₂ SiO ₄	5.1 ± (6)								
50	c-ZrMgO ₂	47.2 ± 0.04	7.62	5.78	6.64	1.3124	4.2942	2.78	1037 ± 12	250 ± 15.16
	MgO	25.6 ± 0.05								
	MgAl ₂ O ₄	26.8 ± 0.03								
	CaWO ₄	0.4 ± 0.03								
60	c-ZrMgO ₂	38.5 ± 0.03	10.38	7.74	6.57	2.4932	4.5432	0.34	736 ± 19	113 ± 3.73
	MgO	10.1 ± 0.02								
	MgAl ₂ O ₄	18.3 ± 0.03								
	m-ZrO ₂	26.5 ± 0.02								
	Si ₁₉₂ O ₃₈₄	6.6 ± 0.03								
70	c-ZrMgO ₂	42.9 ± 0.03	8.78	6.94	6.54	1.7977	4.7018	11.93	777 ± 7	151 ± 6.47
	MgO	0.46 ± 0.07								
	MgAl ₂ O ₄	5.34 ± 0.04								
	m-ZrO ₂	4.3 ± 0.03								
	t-ZrO ₂	47 ± 0.02								
80	c-ZrMgO ₂	44.6 ± 0.02	8.05	6.07	6.34	1.6058	5.0280	1.61	1312 ± 14	211 ± 10.24
	MgO	6.7 ± 0.04								
	MgAl ₂ O ₄	11.9 ± 0.07								
	m-ZrO ₂	7.4 ± 0.05								
	t-ZrO ₂	29.4 ± 0.10								

The increase in the values of mechanical properties may be associated with an elevation in the proportion of the stabilized zirconium dioxide phase c-ZrO₂ and a decrease in the average grain size. As can be seen from Figure 7a the average grain size for the ZrO₂ phase and the MgO, Al₂O₃ phases decreases, and the proportion of the stabilized phase c-ZrO₂ grows in the concentration range of x = 10–40 wt.%. It is important to highlight that despite the increase in porosity from ~10 to 13.5% (see Supplementary Table S4), the values of microhardness and flexural strength grow, indicating that it is the phase composition that determines the strength characteristics of sintered ceramics. It is known from the literature that the microhardness of magnesium oxide and spinel is lower than that of stabilized zirconium dioxide [37,38]. Since the object of study is composite ceramics, then according to the effective medium theory, the properties of the composite will be determined by the concentration of the components of the composite [39]. As the proportion of periclase decreases, the proportion of stabilized zirconium dioxide increases, enhancing the strength of the sintered ceramic. The contribution to the effective values of HV1 and σ_{flex} from the MgAl₂O₄ phase is not decisive due to the fact that its concentration is in the range of 5–25%. Also, in zirconium dioxide, there is a known transformation strengthening mechanism in which there is a phase transition to a monoclinic phase, in which the crack loses its energy and has no ability to propagate further [15,40]. For this reason, the content of stabilized zirconium dioxide can determine the final properties of composite ceramics. An additional mechanism leading to strengthening can be attributed to the following. As the average grain size shrinks, the area of intergranular boundaries, which have a higher concentration of dislocations, grows. High concentrations of dislocations can also stop cracks and increase the values of microhardness and bending strength [41,42].

Since pores are dislocation concentrators, the propagation of cracks will inevitably occur through their accumulations in the volume [43]. This is what causes the low values of mechanical properties of ceramics with concentrations of x = 10–30 wt.% (see Figure 7b and Table 1). The porosity of the above samples is in the range of 10–14%, while HV has a value of less than 1000, and σ_{flex} < 200 MPa. The porosity values above are due

to the asymmetrical wide distribution of particles after annealing and milling (Figure 1). The maximum value of $\sigma_{\text{flex}} = 250$ MPa in Table 1 is directly related to the decrease in porosity in the ceramic disks. For the sample with a concentration of $x = 50$ wt.%, the minimum porosity was found with a value of 3% (Figure 7b). The porosity was calculated using the formula $(1 - \rho_{\text{exp}} / \rho_{\text{theo}}) \cdot 100\%$, where the geometrical density from Figure 3a was used as the experimental density. More information about porosity calculation can be found in Supplementary Tables S2–S4. In addition to low porosity, sintered ceramics with a concentration of $x = 50$ wt.% have a high stabilized zirconium dioxide content, which also determines the highest biaxial flexural strength value. Overall, it can be seen that mechanical characteristics mainly depend on open porosity in sintered ceramics (see Supplementary Table S4). This is due to the connectivity of pores which results in creating a path for crack propagation [43,44].

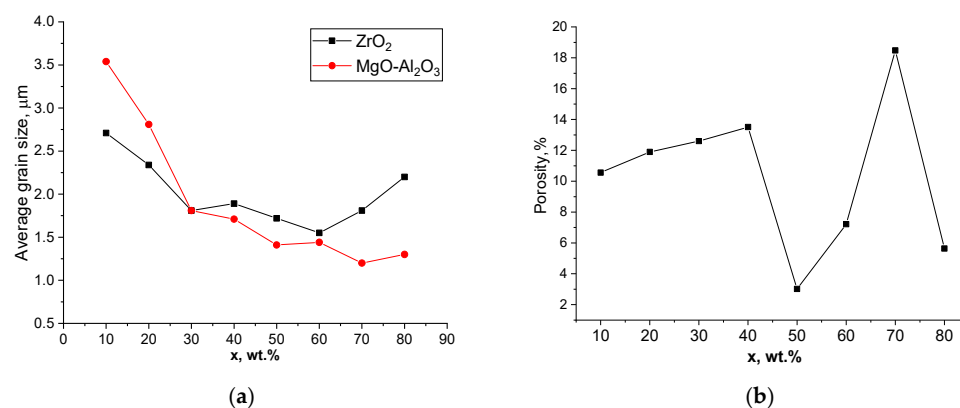


Figure 7. Dependence of the average grain size (a) and total porosity (b) on the starting concentration x .

As the concentration x grows to 60 wt.%, a dramatic decrease in the HV and σ_{flex} values is observed. This change correlates with a sharp increase in the proportion of the monoclinic phase of ZrO_2 , which was found by analyzing the experimental XRD patterns using the Rietveld method (see Table 1). A possible explanation for this effect can be found by analysis of the SEM images (Figure 5). As the study of the microstructure showed for the sample with $x = 60$ wt.%, there is an uneven distribution of the components of the composite ceramics compared to the other samples. Apparently, the clusters of MgO and MgAl_2O_4 grains are the main reason for the transition of the stabilized $c\text{-ZrO}_2$ phase to the monoclinic ZrO_2 . This may occur by the following mechanism. During annealing, Mg atoms possibly volatilize on the grain surface. If there are no MgO periclase grains near the $c\text{-ZrO}_2$ grain, then the diffusion of Mg ions from the grains in the ceramic volume into the ZrO_2 crystal lattice does not occur. This subsequently leads to an increase in the proportion of the monoclinic phase and a decrease in the HV and σ_{flex} values, because of the absence of the stabilizing dopant. Regarding the reasons for the uneven distribution of grains in the microstructure, it can be noted that for the sample $x = 60$ wt.%, a fairly high concentration of MgAl_2O_4 was found in the pre-annealed powders. Since MgAl_2O_4 is a highly stable oxide, then at a sintering temperature of 1500°C , stabilization of zirconium dioxide according to Equation (2) is unlikely, since Mg ions will not leave the MgAl_2O_4 grains [45]. A surprising fact is that for the sample with the highest porosity of 18% ($x = 70$ wt.%), the mechanical property values are comparable with less porous samples. This observation can be explained by the increased content of the tetragonal phase $t\text{-ZrO}_2$, which is characterized by the highest crack resistance among oxide technical ceramics. This surprising fact also points to the decisive contribution of the phase composition to the final properties of $x \cdot \text{ZrO}_2 - (90 - x) \cdot \text{MgO} - 10 \cdot \text{Al}_2\text{O}_3$ ceramics.

A comparison of the measured values of mechanical properties with the results from recent studies is given in Table 2. As can be seen from the table, the values of biaxial flexural strength of some ceramics based on aluminum oxides and zirconium oxide exceed the values obtained in this work by 2–6 times. However, to obtain these ceramics, sintering regimes with much lower heating rates and controlled cooling were used. In addition, most studies used commercial nanoscale or submicron powders as starting materials. The use of micron pre-annealed powders in this work results in high porosity, which reduces the σ_{flex} values. However, conducting experiments with micron powders brings the laboratory experiment closer to production conditions. We believe that by selecting the sintering mode, it is possible to achieve comparable results in such indicators as flexural strength and compressive strength. This assumption is also supported by the fact that the ceramics obtained in this work achieve microhardness values comparable to those obtained by other researchers. The sintering regimes used in this work are suitable for producing porous ceramics, for example for thermal insulation applications.

Table 2. Comparison between composition of ceramics, synthesis method, starting powder size, σ_{flex} , microhardness, and porosity in recent publications and this work.

Composition of Ceramics	Synthesis Method	Starting Powder Size, μm	σ_{flex} , MPa	Microhardness	Porosity, %	Reference
$\text{Al}_2\text{O}_3:\text{ZrO}_2 = 3:1$ with SrO , Cr_2O_3 doping	Conventional processes with pressing and sintering, 1600 °C	0.15–0.20	501 ± 21	$\text{HV}1658 \pm 28$	Low, fully dense	[46]
ZTA- Cr_2O_3	Conventional processes with pressing and sintering, 1450 °C, 2 °C/min heating rate, 3 h hold, 10 °C/min cooling rate	-	546 ± 59	-	4.09	[47]
ZTA-MgO	Conventional processes with pressing and sintering, 1450 °C, 2 °C/min heating rate, 3 h hold, 10 °C/min cooling rate	-	915 ± 41	-	6.17	[47]
ZrO_2 92.5; Al_2O_3 0.07; SiO_2 0.58; MgO 0.14; Na_2O 0.14; K_2O 0.07; SnO_2 0.15; Y_2O_3 4.67; HfO_2 1.64.	Printed via digital light processing, Ramp-up rate 0.2–0.5 °C/min, 1500 °C, 2 h sintering	-	650 ± 76	$\text{HV}1359 \pm 35$	-	[48]
1 mol% Y_2O_3 ; 12 mol% Al_2O_3 ; 1 mol% CoO ; 7 mol% CeO_2 ; 1 mol% Fe_2O_3	Conventional processes with pressing and sintering 1550–1620 °C	0.01–0.04	606 ± 148	-	-	[49]
Zirconia	DLP printed, 30 h of debinding 1100 °C, 1500 °C with dwell time 5 h of sintering	-	1238 ± 327	-	Fully dense	[50]
5Y-PSZ	DLP printed, 30 h of debinding 1100 °C, 1500 °C with dwell time 5 h of sintering	-	1059 ± 178	$\text{HV}1590 \pm 24$	Fully dense	[51]

Table 2. Cont.

Composition of Ceramics	Synthesis Method	Starting Powder Size, μm	σ_{flex} , MPa	Microhardness	Porosity, %	Reference
Zirconia	FDM printed and milled, conventional sintering at 1500 °C with dwell time 2 h	0.4–0.6	1241 ± 200	HV1622 \pm 216	-	[52]
$x\cdot\text{ZrO}_2\text{-(}90-x\text{)}\cdot\text{MgO-}10\cdot\text{Al}_2\text{O}_3$	Conventional processes with pressing and sintering, 10 °C/min, 1500 °C, 5 h	0.8–1.25	250 ± 15.16	HV1312 \pm 14	3–18.5	This Work

The main novelty of this work is the study of the property–composition–structure interactions in multicomponent ceramics $\text{ZrO}_2\text{-MgO-Al}_2\text{O}_3$. In particular, it was found that the formation of the metastable phase $t\text{-ZrO}_2$ and $c\text{-ZrO}_2$ significantly improves the mechanical characteristics and helps to reduce porosity. It was found that despite the high porosity in ceramics with $t\text{-ZrO}_2$ and $c\text{-ZrO}_2$ phases, higher values of bending strength and microhardness are observed compared to dense samples with a high content of the $m\text{-ZrO}_2$ phase.

4. Conclusions

In this work, ternary oxide ceramics with the composition of $x\cdot\text{ZrO}_2\text{-(}90-x\text{)}\cdot\text{MgO-}10\cdot\text{Al}_2\text{O}_3$ ($x = 10\text{--}80$ wt.%) were obtained using the standard ceramic technology with preliminary annealing of powders. A comprehensive study using XRD, SEM and mechanical tests showed that with a change in the concentration of x , the microstructure, microhardness and flexural strength varied significantly. Preliminary annealing at 1300 °C initiates the formation of MgAl_2O_4 and $c\text{-ZrO}_2$ phases, but the concentration of the latter does not exceed 20 wt.% according to the results of Rietveld analysis. After sintering the tablets at 1500 °C, the phase composition changes and the content of the stabilized zirconium dioxide phase can reach 90 wt.%. At low x concentrations in the range of 10–40 wt.%, the high porosity of the ceramics is due to the large initial size of the MgO particles. Despite the relatively high porosity, the high HV and σ_{flex} values are mainly due to the change in phase composition. With a decrease in the proportion of periclase MgO and an increase in the proportion of $c\text{-ZrO}_2$ at a concentration of $x = 50$ wt.%, high values of microhardness of 1000 HV and biaxial bending strength of 250 MPa were found. In the microstructure of sintered ceramic disks above the concentration of $x = 10$ wt.%, ZrO_2 grains with a developed morphology, which arises due to the volatilization of Mg atoms and eutectoid decomposition, were found. The uneven distribution of grains of different phases in the volume leads to a significant deterioration in mechanical properties. This is due to the formation of an unstabilized $m\text{-ZrO}_2$ phase in the composition of the final ceramics.

Supplementary Materials: The following supporting information can be downloaded at <https://www.mdpi.com/article/10.3390/ceramics8030114/s1>, Figure S1: Size distribution of initial powders obtained by SEM (a), (c), (e) and by laser analyzer (b), (d), (f) for ZrO_2 , MgO and Al_2O_3 , respectively; Figure S2: SEM images of starting powders ZrO_2 (a), MgO (b) and Al_2O_3 (c); Figures S3–S10: XRD patterns with corresponding phases from PDF database (a) and results of Rietveld fitting (b) for the samples with concentration $x = 10\text{--}80$; Figures S11–S18: Surface EDX maps for $x = 10\text{--}80$ wt.%. (a) SEM; (b) Zr; (c) Al; (d) Mg; Figure S19: Representation view of the indents; Table S1: Values of geometrical parameters of sintered tablets (R —radius of tablet, t —thickness of tablet); Table S2: Values of theoretical density used for effective theoretical density calculations; Table S3: Comparison between geometrical density (ρ_{exp}), Archimedes density (ρ_A) and effective theoretical density (ρ_{theo}) of sintered disks; Table S4: Comparison between total porosity, closed porosity and open porosity of sintered disks.

Author Contributions: Conceptualization of conducted research was performed by R.S.; Y.G. developed the research methodology; Validation of results was performed by M.K.; Formal analysis was performed by R.S.; Investigation and samples preparation were performed by Y.G., S.M. and R.S.; Resources for conducting research were obtained by M.K.; Data collection was performed by Y.G. and M.K.; Original draft preparation was performed by R.S.; Review and editing of the manuscript were performed by R.S. and M.K.; All figures preparation and visualization were performed by Y.G., R.S. and M.K.; Supervision was performed by R.S. All authors have read and agreed to the published version of the manuscript.

Funding: This research was funded by the Committee of Science of the Ministry of Science and Higher Education of the Republic of Kazakhstan (grant no. BR21882390).

Institutional Review Board Statement: Not applicable.

Informed Consent Statement: Not applicable.

Data Availability Statement: The data presented in this study are available on request from the corresponding author.

Conflicts of Interest: The authors declare no conflicts of interest.

References

1. Evans, A.G. Perspective on the Development of High-Toughness Ceramics. *J. Am. Ceram. Soc.* **1990**, *73*, 187–206. [\[CrossRef\]](#)
2. Shvydyuk, K.O.; Nunes-Pereira, J.; Rodrigues, F.F.; Silva, A.P. Review of Ceramic Composites in Aeronautics and Aerospace: A Multifunctional Approach for TPS, TBC and DBD Applications. *Ceramics* **2023**, *6*, 195–230. [\[CrossRef\]](#)
3. Kostishin, V.G.; Korovushkin, V.V.; Pokholok, K.V.; Trukhanov, A.V.; Isaev, I.M.; Mironovich, A.Y.; Darwish, M.A. Cation Distribution and Magnetic Properties of Polycrystalline Hexagonal BaFe₁₂–XSnxO₁₉ Ferrites. *Phys. Solid State* **2021**, *63*, 1680–1689. [\[CrossRef\]](#)
4. Boniecki, M.; Sadowski, T.; Gołębiewski, P.; Węglarz, H.; Piątkowska, A.; Romaniec, M.; Krzyżak, K.; Łosiewicz, K. Mechanical Properties of Alumina/Zirconia Composites. *Ceram. Int.* **2020**, *46*, 1033–1039. [\[CrossRef\]](#)
5. Kelly, J.R.; Denry, I. Stabilized Zirconia as a Structural Ceramic: An Overview. *Dent. Mater.* **2008**, *24*, 289–298. [\[CrossRef\]](#)
6. Cao, X.Q.; Vassen, R.; Stoeber, D. Ceramic Materials for Thermal Barrier Coatings. *J. Eur. Ceram. Soc.* **2004**, *24*, 1–10. [\[CrossRef\]](#)
7. Twomey, B.; de Faoite, D.; Doherty, K.A.J.; Stanton, K.T. Ceramics in Space Applications. *Encycl. Mater. Tech. Ceram. Glas.* **2021**, *2*, 359–379. [\[CrossRef\]](#)
8. Sequeira, S.; Fernandes, M.H.; Neves, N.; Almeida, M.M. Development and Characterization of Zirconia–Alumina Composites for Orthopedic Implants. *Ceram. Int.* **2017**, *43*, 693–703. [\[CrossRef\]](#)
9. Meir, S.; Kalabukhov, S.; Frage, N.; Hayun, S. Mechanical Properties of Al₂O₃/Ti Composites Fabricated by Spark Plasma Sintering. *Ceram. Int.* **2015**, *41*, 4637–4643. [\[CrossRef\]](#)
10. Wahsh, M.M.S.; Khattab, R.M.; Awaad, M. Thermo-Mechanical Properties of Mullite/Zirconia Reinforced Alumina Ceramic Composites. *Mater. Des.* **2012**, *41*, 31–36. [\[CrossRef\]](#)
11. Rittidech, A.; Somrit, R.; Tunkasiri, T. Effect of Adding Y₂O₃ on Structural and Mechanical Properties of Al₂O₃–ZrO₂ Ceramics. *Ceram. Int.* **2013**, *39*, S433–S436. [\[CrossRef\]](#)
12. Malka, I.E.; Daneliska, A.; Kimmel, G. The Influence of Al₂O₃ Content on ZrO₂–Al₂O₃ Nanocomposite Formation—The Comparison between Sol-Gel and Microwave Hydrothermal Methods. *Mater. Today Proc.* **2016**, *3*, 2713–2724. [\[CrossRef\]](#)
13. Burger, W.; Kiefer, G. Alumina, Zirconia and Their Composite Ceramics with Properties Tailored for Medical Applications. *J. Compos. Sci.* **2021**, *5*, 306. [\[CrossRef\]](#)
14. Kozlovskiy, A.L.; Konuhova, M.; Borgekov, D.B.; Anatoli, P.I. Study of Irradiation Temperature Effect on Radiation-Induced Polymorphic Transformation Mechanisms in ZrO₂ Ceramics. *Opt. Mater.* **2024**, *156*, 115994. [\[CrossRef\]](#)
15. Chevalier, J.; Gremillard, L.; Virkar, A.V.; Clarke, D.R. The Tetragonal-Monoclinic Transformation in Zirconia: Lessons Learned and Future Trends. *J. Am. Ceram. Soc.* **2009**, *92*, 1901–1920. [\[CrossRef\]](#)
16. Sommer, F.; Landfried, R.; Kern, F.; Gadow, R. Mechanical Properties of Zirconia Toughened Alumina with 10–24 Vol.% 1.5 Mol% Y-TZP Reinforcement. *J. Eur. Ceram. Soc.* **2012**, *32*, 3905–3910. [\[CrossRef\]](#)
17. Łabuz, A.; Lach, R.; Raczka, M.; Wójtowicz, B.; Pyda, W. Processing and Characterization of Ca-TZP Nanoceramics. *J. Eur. Ceram. Soc.* **2015**, *35*, 3943–3947. [\[CrossRef\]](#)
18. Gómez-Rodríguez, C.; García-Quinonez, L.V.; Aguilar-Martínez, J.A.; Castillo-Rodríguez, G.A.; Rodríguez-Castellanos, E.A.; López-Perales, J.F.; Mendivil-Palma, M.I.; Verdeja, L.F.; Fernández-González, D. MgO–ZrO₂ Ceramic Composites for Silicomanganese Production. *Materials* **2022**, *15*, 2421. [\[CrossRef\]](#)

19. Yi, H.; Che, J.; Liang, G.; Liu, X. Effect of Rare Earth Elements on Stability and Sintering Resistance of Tetragonal Zirconia for Advanced Thermal Barrier Coatings. *Crystals* **2021**, *11*, 287. [\[CrossRef\]](#)
20. Wang, J.; Chen, M.; Sun, J.; Hu, M.; Lu, X.; Shu, C.; Zhang, H.; Wang, Y. Phase Stability and Thermophysical Properties of CeO₂-Re₂O₃ (ReEu, Gd, Dy, Y, Er, Yb) Co-Stabilised Zirconia. *Ceram. Int.* **2023**, *49*, 21634–21644. [\[CrossRef\]](#)
21. Ramesh, S.; Sara Lee, K.Y.; Tan, C.Y. A Review on the Hydrothermal Ageing Behaviour of Y-TZP Ceramics. *Ceram. Int.* **2018**, *44*, 20620–20634. [\[CrossRef\]](#)
22. Roy, M.E.; Whiteside, L.A.; Katerberg, B.J.; Steiger, J.A. Phase Transformation, Roughness, and Microhardness of Artificially Aged Yttria- and Magnesia-Stabilized Zirconia Femoral Heads. *J. Biomed. Mater. Res. A* **2007**, *83A*, 1096–1102. [\[CrossRef\]](#) [\[PubMed\]](#)
23. Rejab, N.A.; Azhar, A.Z.A.; Kian, K.S.; Ratnam, M.M.; Ahmad, Z.A. Effects of MgO Addition on the Phase, Mechanical Properties, and Microstructure of Zirconia-Toughened Alumina Added with CeO₂ (ZTA–CeO₂) Ceramic Composite. *Mater. Sci. Eng. A* **2014**, *595*, 18–24. [\[CrossRef\]](#)
24. Kosmač, T.; Wallace, J.; Claussen, N. Influence of MgO Additions on the Microstructure and Mechanical Properties of Al₂O₃-ZrO₂ Composites. *J. Am. Ceram. Soc.* **1982**, *65*, c66–c67. [\[CrossRef\]](#)
25. Ngashangua, S.; Vasanthavel, S.; Ponnillavan, V.; Kannan, S. Effect of MgO Additions on the Phase Stability and Degradation Ability in ZrO₂-Al₂O₃ Composite Systems. *Ceram. Int.* **2015**, *41*, 3814–3821. [\[CrossRef\]](#)
26. Sarkar, M.; Dutta, S.; Chakraborty, S.S.; Mandal, N. Grain Size Distribution Analysis of MgO and VC Inhibited Zirconia Toughened Alumina Ceramics Using Digital Image Processing. *Mater. Today Commun.* **2024**, *39*, 108665. [\[CrossRef\]](#)
27. Azhar, A.Z.A.; Mohamad, H.; Ratnam, M.M.; Ahmad, Z.A. Effect of MgO Particle Size on the Microstructure, Mechanical Properties and Wear Performance of ZTA–MgO Ceramic Cutting Inserts. *Int. J. Refract. Met. Hard Mater.* **2011**, *29*, 456–461. [\[CrossRef\]](#)
28. Meena, K.L.; Karunakar, D.B. Effect of ZrO₂ and MgO Added in Alumina on the Physical and Mechanical Properties of Spark Plasma Sintered Nanocomposite. *Int. J. Refract. Met. Hard Mater.* **2019**, *81*, 281–290. [\[CrossRef\]](#)
29. Pavlyuchkov, D.; Savinykh, G.; Fabrichnaya, O. Experimental Investigation and Thermodynamic Modeling of the ZrO₂-MgO-Al₂O₃ System. *J. Eur. Ceram. Soc.* **2014**, *34*, 1397–1408. [\[CrossRef\]](#)
30. ISO 6872:2024; Dentistry—Ceramic Materials. International Organization for Standardization: Geneva, Switzerland, 2024.
31. Waters, M.J.; Rondinelli, J.M.; Cuevas, J.L.; Courel Piedrahita, M.; Feddi, E.; Buyakova, S.P.; Kalatur, E.S.; Buyakov, A.S.; Kulkov, S.S. Structure and Properties of ZrO₂-MgO Powders. *IOP Conf. Ser. Mater. Sci. Eng.* **2016**, *123*, 012040. [\[CrossRef\]](#)
32. Duwez, P.; Odell, F.; Brown, F.H. Stabilization of Zirconia with Calcia and Magnesia. *J. Am. Ceram. Soc.* **1952**, *35*, 107–113. [\[CrossRef\]](#)
33. Toraya, H. Whole-Powder-Pattern Fitting without Reference to a Structural Model: Application to X-Ray Powder Diffraction Data. *J. Appl. Crystallogr.* **1986**, *19*, 440–447. [\[CrossRef\]](#)
34. Echigoya, J.; Sasai, K.S.H. Microstructural Change of 11 Mol% MgO-ZrO₂ by Aging. *Trans. Jpn. Inst. Met.* **1988**, *29*, 561–569. [\[CrossRef\]](#)
35. Śniezek, E.; Szczerba, J.; Stoch, P.; Prorok, R.; Jastrzebska, I.; Bodnar, W.; Burkel, E. Structural Properties of MgO-ZrO₂ Ceramics Obtained by Conventional Sintering, Arc Melting and Field Assisted Sintering Technique. *Mater. Des.* **2016**, *99*, 412–420. [\[CrossRef\]](#)
36. Keerthana, L.; Sakthivel, C.; Prabha, I. MgO-ZrO₂ Mixed Nanocomposites: Fabrication Methods and Applications. *Mater. Today Sustain.* **2019**, *3–4*, 100007. [\[CrossRef\]](#)
37. Bron, V.A.; Perepelitsyn, V.A.; Raeva, I.S.; Adel', T.A.; Deryavina, V.I. Microhardness of Fused Periclase. *Refractories* **1984**, *25*, 198–202. [\[CrossRef\]](#)
38. Gajdowski, C.; D'Elia, R.; Faderl, N.; Böhmeler, J.; Lorgouilloux, Y.; Lemonnier, S.; Leriche, A. Mechanical and Optical Properties of MgAl₂O₄ Ceramics and Ballistic Efficiency of Spinel Based Armour. *Ceram. Int.* **2022**, *48*, 18199–18211. [\[CrossRef\]](#)
39. Wang, M.; Pan, N. Predictions of Effective Physical Properties of Complex Multiphase Materials. *Mater. Sci. Eng. R Rep.* **2008**, *63*, 1–30. [\[CrossRef\]](#)
40. Patil, R.N.; Subbarao, E.C. Monoclinic-Tetragonal Phase Transition in Zirconia: Mechanism, Pretransformation and Coexistence. *Acta Crystallogr. Sect. A* **1970**, *26*, 535–542. [\[CrossRef\]](#)
41. Seidel, J.; Claussen, N.; Rödel, J. Reliability of Alumina Ceramics: Effect of Grain Size. *J. Eur. Ceram. Soc.* **1995**, *15*, 395–404. [\[CrossRef\]](#)
42. Kambale, K.R.; Mahajan, A.; Butee, S.P. Effect of Grain Size on the Properties of Ceramics. *Met. Powder Rep.* **2019**, *74*, 130–136. [\[CrossRef\]](#)
43. Shakirzyanov, R.I.; Volodina, N.O.; Kozlovskiy, A.L.; Zdorovets, M.V.; Shlimas, D.I.; Borgekov, D.B.; Garanin, Y.A. Study of the Structural, Electrical, and Mechanical Properties and Morphological Features of Y-Doped CeO₂ Ceramics with Porous Structure. *J. Compos. Sci.* **2023**, *7*, 411. [\[CrossRef\]](#)
44. Klym, H.; Karbovnyk, I.; Piskunov, S.; Popov, A.I. Positron Annihilation Lifetime Spectroscopy Insight on Free Volume Conversion of Nanostructured MGAL₂O₄ Ceramics. *Nanomaterials* **2021**, *11*, 3373. [\[CrossRef\]](#)

45. Ma, Y.; Liu, X. Kinetics and Thermodynamics of Mg-Al Disorder in MgAl_2O_4 -Spinel: A Review. *Molecules* **2019**, *24*, 1704. [[CrossRef](#)]
46. Yan, X.; Zhang, B.; Wang, Y.; Hong, H.; Li, H.; Cheng, B.; Yang, J.; Li, B.; Wang, X. Preparation of High-Performance Zirconia Toughened Alumina Doped with Cr_2O_3 and SrO for Artificial Joints by Spray Granulation. *Ceram. Int.* **2024**, *50*, 28641–28651. [[CrossRef](#)]
47. Saggiaro, A.C.B.; Fernandes, L.; De Oliveira Carlos Villas-Bôas, M.; Salomão, R.; Pinelli, L.A.P. Processing and Characterization of a Novel ZTA-MGO for Dental Applications. *Mater. Res.* **2025**, *28*, e20240404. [[CrossRef](#)]
48. Cai, H.; Lee, M.-Y.; Jiang, H.B.; Kwon, J.-S. Influence of Various Cleaning Solutions on the Geometry, Roughness, Gloss, Hardness, and Flexural Strength of 3D-Printed Zirconia. *Sci. Rep.* **2024**, *14*, 22551. [[CrossRef](#)] [[PubMed](#)]
49. Kulyk, V.; Vasylyv, B.; Duriagina, Z.; Lyutyty, P.; Vavruk, V.; Kostyryzhev, A. The Effect of Sintering Temperature on Phase-Related Peculiarities of the Microstructure, Flexural Strength, and Fracture Toughness of Fine-Grained ZrO_2 - Y_2O_3 - Al_2O_3 - CoO - CeO_2 - Fe_2O_3 Ceramics. *Crystals* **2024**, *14*, 175. [[CrossRef](#)]
50. Zenthöfer, A.; Ilani, A.; Schmitt, C.; Rammelsberg, P.; Hetzler, S.; Rues, S. Biaxial Flexural Strength of 3D-Printed 3Y-TZP Zirconia Using a Novel Ceramic Printer. *Clin. Oral Investig.* **2024**, *28*, 145. [[CrossRef](#)]
51. Hetzler, S.; Hinzen, C.; Rues, S.; Schmitt, C.; Rammelsberg, P.; Zenthöfer, A. Biaxial Flexural Strength and Vickers Hardness of 3D-Printed and Milled 5Y Partially Stabilized Zirconia. *J. Funct. Biomater.* **2025**, *16*, 36. [[CrossRef](#)]
52. Hajjaj, M.S.; Alamoudi, R.A.A.; Babeer, W.A.; Rizg, W.Y.; Basalah, A.A.; Alzahrani, S.J.; Yeslam, H.E. Flexural Strength, Flexural Modulus and Microhardness of Milled vs. Fused Deposition Modeling Printed Zirconia; Effect of Conventional vs. Speed Sintering. *BMC Oral Health* **2024**, *24*, 38. [[CrossRef](#)] [[PubMed](#)]

Disclaimer/Publisher’s Note: The statements, opinions and data contained in all publications are solely those of the individual author(s) and contributor(s) and not of MDPI and/or the editor(s). MDPI and/or the editor(s) disclaim responsibility for any injury to people or property resulting from any ideas, methods, instructions or products referred to in the content.